

Numerical solution of light scattered from and transmitted through a rough dielectric surface with applications to periodic roughness and isolated structures

Wenbo Sun

Center for Atmospheric Sciences, Hampton University, Hampton, Virginia 23668

Gorden Videen

U.S. Army Research Laboratory, Adelphi, Maryland 20783

Bing Lin and Yongxiang Hu

NASA Langley Research Center, Hampton, Virginia 23681

Submitted to Applied Optics

July 5, 2006

Corresponding author address: Dr. Wenbo Sun, Mail Stop 420, NASA Langley Research Center, Hampton, VA 23681-0001. E-mail: w.sun@larc.nasa.gov

Abstract

Light scattering and transmission by rough surfaces are of considerable interest in a variety of applications including remote sensing and characterization of surfaces. In this work, the finite-difference time domain technique is applied to calculate the scattered and transmitted electromagnetic fields of an infinite periodic rough surface. The elements of Mueller matrix for scattered light are calculated by an integral of the near fields over a significant number of periods of the surface. The normalized Mueller matrix elements of the scattered light and the spatial distribution of the transmitted flux for a monolayer of micron-sized dielectric spheres on a silicon substrate are presented. The numerical results show that the nonzero Mueller matrix elements of the system of the monolayer of dielectric spheres on a silicon substrate have specific maxima at some scattering angles. These maxima may be used in characterization of the feature of the system. For light transmitted through the monolayer of spheres, our results show that the transmitted energy focuses around the ray passing through centers of the spheres. At other locations, the transmitted flux is very small. The technique also may be used to calculate the perturbation of the electromagnetic field due to the presence of an isolated structure on the substrate.

Key words: Light scattering, transmission, finite-difference time domain, microstructure, rough surface.

1. Introduction

Understanding of electromagnetic scattering from surfaces is essential to interpretation of radar observation of solid bodies, radio wave surface sounding, and many terrestrial or extraterrestrial remote sensing problems¹. The scattering of electromagnetic waves from, and their transmission through, rough surfaces has also been of considerable interest in applications such as detection of surface defects or contamination², characterization of nanometer-sized particles in crystalline structures³, and telecommunications⁴. The frequently used algorithms on wave scattering from rough surfaces can be divided into two categories. The first one is analytical approximate approaches, such as the small perturbation model (SPM)⁵⁻⁸, the Kirchhoff approximation (KA)⁹⁻¹¹, the integral equation method (IEM)¹²⁻¹⁵, and other methods¹⁶. The second category of the light scattering solutions is based on sparse-matrix grid numerical solutions such as the finite element method (FEM)^{17,18} and the finite-difference time domain (FDTD) technique¹⁹⁻²¹. The approximate approaches for light scattering and transmission by rough surfaces have limitations in their applicability. For example, the computed scattering field of the SPM is only valid for the contribution from surfaces with roughness scale much smaller than the incident wavelength, whereas the KA is only valid when surface roughness level is much greater than the wavelength. When the surface roughness scale is similar to the wavelength such as the sea surface capillary waves under millimeter wave radar incidence or a micron-sized particle layer in a visible laser illumination, neither the SPM nor the KA can be applied to calculate the scattering or transmission of the light by the surface. Although the IEM model was developed to bridge the gap between the SPM and the KA models, as an approximate method which is essentially a second iteration of the

iterative KA, its accuracy is still in progress²²⁻²⁵. Therefore, when the surface roughness scale is similar to the wavelength, accurate approaches based on numerical solutions of the Maxwell's equations such as the FDTD technique are usually used although these methods require large computational resources²⁶⁻³¹. In this study, a FDTD method is applied to calculate the scattered and transmitted electromagnetic fields of an infinite three-dimensional periodic rough surface. In Section 2, the FDTD algorithm with periodic boundary conditions²⁶ and uniaxial perfectly matched layer (UPML) absorbing boundary conditions (ABC)^{32, 33} are introduced. The Section 3 develops an approach to calculate the scattering properties for the surface. Features of light scattered from and transmitted through a monolayer of dielectric spheres on a silicon substrate are presented in Section 4. Summary and conclusions are given at the end of this report.

2. The finite-difference time domain method

The FDTD technique calculates electromagnetic scattering and transmission by a material interface in the time domain by directly solving the finite-differenced Maxwell's equations. In this technique, the continuous space and time (x, y, z, t) is replaced by discrete spatial and temporal points, and the field components are calculated only at these discrete points. The magnetic and electric field components are on different spatial points and are evaluated at alternating half-time steps. A time-stepping iteration is used to simulate the field variation with time. The time series at each data collection grid point are transformed into the fields in frequency domain using the discrete Fourier transform (DFT). The scattering and absorption quantities are calculated using the fields in frequency domain. For example, in a Cartesian grid system the x components of magnetic and electric fields are in the forms

$$H_x^{n+1/2}(i, j+1/2, k+1/2) = H_x^{n-1/2}(i, j+1/2, k+1/2) + \frac{\Delta t}{\mu(i, j+1/2, k+1/2)\Delta s} \quad (1a)$$

$$\times [E_y^n(i, j+1/2, k+1) - E_y^n(i, j+1/2, k) + E_z^n(i, j, k+1/2) - E_z^n(i, j+1, k+1/2)],$$

$$E_x^{n+1}(i+1/2, j, k) = \exp\left[-\frac{\varepsilon_i(i+1/2, j, k)}{\varepsilon_r(i+1/2, j, k)}\omega\Delta t\right]E_x^n(i+1/2, j, k) +$$

$$\exp\left[-\frac{\varepsilon_i(i+1/2, j, k)}{\varepsilon_r(i+1/2, j, k)}\omega\Delta t/2\right]\frac{\Delta t}{\varepsilon_r(i+1/2, j, k)\Delta s} \quad (1b)$$

$$\times [H_y^{n+1/2}(i+1/2, j, k-1/2) - H_y^{n+1/2}(i+1/2, j, k+1/2)$$

$$+ H_z^{n+1/2}(i+1/2, j+1/2, k) - H_z^{n+1/2}(i+1/2, j-1/2, k)],$$

where E_x , E_y , E_z and H_x , H_y , H_z denote electric and magnetic components, respectively; the time step is denoted by integer n ; ω is the angular frequency of the light; Δs and Δt denote the cubic cell size and time increment, respectively; ε_i and ε_r are the local imaginary and real permittivity, respectively; and μ is the local permeability. The material surface is generated by assigning different permittivity (and permeability for ferromagnetic material) at different grid points. To guarantee the numerical stability of the FDTD scheme, we use a time step $\Delta t = \Delta s/(2c)$, where c is the light speed in free space. Therefore, the light propagates half grid cell in the time step. This is a more strict stability criterion than the Courant-Friedrichs-Levy condition³⁴. In the FDTD algorithm, a cubic grid cell is a unit computational domain. In this study, the positions of the magnetic and electric field components on a cubic grid cell are identical to those illustrated in Sun et al.³⁵.

Figure 1 illustrates an example of light scattering by a rough surface: A flat silicon substrate with micron-scale particles on it under visible light illumination. Also shown in this figure are coordinate systems used in derivation of the light scattering formulae. We assume the surface $z = f(x, y)$ stretches infinitely in x and y directions. The roughness features (z) of the surface are repetitive in both x and y directions. The physical modeling for the FDTD algorithm is illustrated in Fig. 2. We assume the incident electromagnetic waves propagate along z -direction. In the incidence direction, the computational domain

is truncated by the UPML ABC^{32, 33}. At sides $i = i_a$ and i_b and $j = j_a$ and j_b , periodic boundary conditions can be applied, e.g. for Ex and Hx components

$$H_x^{n+1/2}(i_b, j + 1/2, k + 1/2) \leftarrow H_x^{n+1/2}(i_a, j + 1/2, k + 1/2), \quad (2a)$$

$$H_x^{n+1/2}(i, j_b + 1/2, k + 1/2) \leftarrow H_x^{n+1/2}(i, j_a + 1/2, k + 1/2), \quad (2b)$$

$$E_x^{n+1}(i_a + 1/2, j, k) \leftarrow E_x^{n+1}(i_b + 1/2, j, k), \quad (2c)$$

$$E_x^{n+1}(i + 1/2, j_a, k) \leftarrow E_x^{n+1}(i + 1/2, j_b, k), \quad (2d)$$

where the arrow “ \leftarrow ” denotes the assignment of the value of the field component at its right side to the field component at its left side.

In this study, we use the total- and scattered-field formulation^{36, 37} to excite the magnetic and electric fields to simulate a linearly polarized plane wave propagating to the target surface. In this formulation, the electric field is excited on an inner surface $k = k_a$ between the material surface and the UPML as shown in Fig. 2. The magnetic field is excited at $k = k_a - 1/2$. Due to the periodic boundary conditions at sides $i = i_a$ and i_b and $j = j_a$ and j_b and because the magnetic wave is excited half-cell-size behind the electric wave, the excited electromagnetic waves can only propagate in the positive z direction. Note that for non-normal incidence cases at discrete incident angles, if the incident angle θ_0 and the length of the repeating period of the surface D satisfy $m\lambda_0 = D \sin \theta_0$, where m denotes an integer and λ_0 is the incident wavelength, the periodic boundary conditions exemplified by Eqs.(2a)-(2d) will still be valid. However, the excitation of non-normal plane incident wave for an infinite periodic surface will be relatively complicated if not impossible. For simplicity, in this study only normal incidence is considered. Therefore, the whole computational domain is divided by the inner surface into two zones: the scattered-field zone and the total field zone as shown in Fig. 2. For example, the x components of the magnetic and electric fields are implemented as follows^{38, 39}:

$$H_x^{n+1/2}(i, j, k_a - 1/2) = \{H_x^{n+1/2}(i, j, k_a - 1/2)\}_{(1a)} - \frac{\Delta t}{\mu_0 \Delta s} E_{y,inc}^n(i, j, k_a), \quad (3a)$$

where $i = i_a, \dots, i_b; j = j_a + 1/2, \dots, j_b - 1/2$ and

$$E_x^{n+1}(i, j, k_a) = \{E_x^{n+1}(i, j, k_a)\}_{(1b)} + \frac{\Delta t}{\epsilon_0 \Delta s} H_{y,inc}^{n+1/2}(i, j, k_a - 1/2), \quad (3b)$$

where $i = i_a + 1/2, \dots, i_b - 1/2; j = j_a, \dots, j_b$.

In Eqs. (3a) and (3b), $\{H_x^{n+1/2}(i, j, k)\}_{(1a)}$ and $\{E_x^{n+1}(i, j, k)\}_{(1b)}$ denote the magnetic and electric fields directly from Eqs.(1a) and (1b), respectively. The incident field $E_{y,inc}^n, E_{z,inc}^n$ and $H_{y,inc}^{n+1/2}, H_{z,inc}^{n+1/2}$ in Eqs.(3a) and (3b) are from the linear interpolation of the fields produced by an auxiliary one-dimensional FDTD scheme^{38, 39}

$$H_{inc}^{n+1/2}(m+1/2) = H_{inc}^{n-1/2}(m+1/2) + \frac{\Delta t}{\mu_0 \Delta s} \times [E_{inc}^n(m) - E_{inc}^n(m+1)], \quad (4a)$$

$$E_{inc}^{n+1}(m) = E_{inc}^n(m) + \frac{\Delta t}{\epsilon_0 \Delta s} \times [H_{inc}^{n+1/2}(m-1/2) - H_{inc}^{n+1/2}(m+1/2)]. \quad (4b)$$

This scheme simulates the incident plane wave's propagation on the one-dimensional grid stretching from grid $m = 0$ to $m = m_{max}$. Because the light propagates half grid cell in a time step, m_{max} is given as half of the total number of the simulation time steps. In this way, no reflection occurs at the forward end of the one-dimensional computational domain before the simulation ends³⁹. A Gaussian-pulse hard wave source is positioned at the one-dimensional grid point $m = 2$ in the form

$$E_{inc}^n(m=2) = \exp\left[-\left(\frac{t}{30 \Delta t} - 5\right)^2\right]. \quad (5)$$

Using the hard wave source rather than a soft one at $m = 2$, the field at the grid points $m = 0$ and 1 will not affect the field at the grid points $m \geq 2$, therefore no boundary condition need to be considered at this grid end³⁹.

3. Formulation of the scattering properties

In this study, we follow the convention in Bohren and Huffman⁴¹ for the relation between incident and scattered Stokes parameters by Mueller matrix as

$$\begin{bmatrix} I_s \\ Q_s \\ U_s \\ V_s \end{bmatrix} = \frac{1}{k^2 R^2} \begin{bmatrix} S_{11} & S_{12} & S_{13} & S_{14} \\ S_{21} & S_{22} & S_{23} & S_{24} \\ S_{31} & S_{32} & S_{33} & S_{34} \\ S_{41} & S_{42} & S_{43} & S_{44} \end{bmatrix} \begin{bmatrix} I_0 \\ Q_0 \\ U_0 \\ V_0 \end{bmatrix}, \quad (6)$$

where k is the wave number and $R = |\mathbf{R}|$ where \mathbf{R} denotes the position vector of the observation point. The Mueller matrix contains all the information on light scattered from a rough surface. For a full formulation of the scattering properties of a surface, the Mueller matrix is derived from the fields calculated by the FDTD method on a virtual surface in the scattered-field zone as shown in Fig. 2. For an infinite surface scattering problem, this virtual surface must also be infinite. However, the near-field to far-field transformation by an integral of the fields on an infinite surface is computationally impractical. In this study, we derive the Mueller matrix using the magnetic and electric fields in frequency domain on the virtual surface corresponding to the period of the material surface.

On the virtual surface, the tangential components of the scattered near fields in frequency domain \mathbf{E}^s and \mathbf{H}^s are first calculated using the FDTD method. The scattered far fields can be computed in terms of the equivalent surface electric current \mathbf{J} and magnetic current \mathbf{M} on the virtual surface. The equivalent surface currents are computed by

$$\mathbf{J} = \mathbf{n} \times \mathbf{H}^s, \quad (7a)$$

$$\mathbf{M} = -\mathbf{n} \times \mathbf{E}^s, \quad (7b)$$

where \mathbf{n} is the outward unit normal vector on the virtual surface. In a spherical coordinate as shown in Fig. 1, the scattered electric far field components for θ and ϕ polarizations are given as follows²¹:

$$E_{\theta} \approx -\frac{ik \exp(-ikR)}{4\pi R} (L_{\theta} + \eta_0 N_{\theta}), \quad (8a)$$

$$E_{\phi} \approx +\frac{ik \exp(-ikR)}{4\pi R} (L_{\phi} - \eta_0 N_{\phi}), \quad (8b)$$

where $\eta_0 = \sqrt{\frac{\mu_0}{\epsilon_0}}$ is the intrinsic impedance of free space and L_{θ}, L_{ϕ} and N_{θ}, N_{ϕ} are the θ and ϕ components of the following vectors

$$\mathbf{L} = \iint_s (\mathbf{x}M_x + \mathbf{y}M_y + \mathbf{z}M_z) \exp(i\mathbf{k}\mathbf{r}' \cdot \mathbf{r}) ds', \quad (9a)$$

$$\mathbf{N} = \iint_s (\mathbf{x}J_x + \mathbf{y}J_y + \mathbf{z}J_z) \exp(i\mathbf{k}\mathbf{r}' \cdot \mathbf{r}) ds', \quad (9b)$$

where \mathbf{x} , \mathbf{y} , and \mathbf{z} denote the unit vector in x, y and z directions, respectively; \mathbf{r} denotes the unit vector in the scattering direction; \mathbf{r}' is the vector for the currents' position on the virtual surface s ; M_x, M_y, M_z and J_x, J_y, J_z are the components of magnetic current \mathbf{M} and electric current \mathbf{J} , respectively. For a reasonable accuracy in calculations of the scattering properties from an infinite surface, the integral area s in Eqs.(9a) and (9b) must be many periods of the virtual surface (See Section 4). Although the FDTD only computes the magnetic and electric fields on one period of the virtual surface, the fields on this single period of virtual surface can be repeatedly used in Eqs.(9a) and (9b) for other periods of the virtual surface s . However, when many periods are involved in the calculation Eqs. (9a) and (9b) in their original forms are very time-consuming. Due to the periodic nature of the studied surface and the scattered light, Eqs.9(a) and 9(b) can be simplified to the following computationally efficient forms:

$$\mathbf{L} = \delta \iint_{s_0} (\mathbf{x}M_x + \mathbf{y}M_y + \mathbf{z}M_z) \exp(i\mathbf{k}\mathbf{r}' \cdot \mathbf{r}) ds', \quad (10a)$$

$$\mathbf{N} = \delta \iint_{s_0} (\mathbf{x}J_x + \mathbf{y}J_y + \mathbf{z}J_z) \exp(i\mathbf{k}\mathbf{r}' \cdot \mathbf{r}) ds', \quad (10b)$$

where s_0 denotes the area of single period of the virtual surface s ; δ is a factor accounting for the contributions from all periods of the infinite surface in a form

$$\delta = \sum_{m=-\infty}^{\infty} \sum_{n=-\infty}^{\infty} \exp[i\mathbf{k}\mathbf{r} \cdot (m\mathbf{p}_x, n\mathbf{p}_y, 0)], \quad (11)$$

where p_x and p_y are the period lengths in x and y directions, respectively. Related to scattering intensity, δ is a two-dimensional delta function of scattering angle, which gives infinitely large value at backscattering direction. In practice, the summation of Eq. (11) cannot be done for infinite m and n . The cut-off for m and n will cause errors in δ values and result in errors in the calculated Mueller matrix elements. However, the ratios of Mueller matrix elements to S_{11} will not be affected by $|\delta|^2$ since this factor exists in all of the elements.

Given the Cartesian geometry of the basic FDTD grid and its near-to-far-field transformation virtual surface s , vectors \mathbf{L} and \mathbf{N} are first calculated in rectangular coordinates and then transformed to spherical coordinates to get L_θ, L_ϕ and N_θ, N_ϕ needed in Eqs.(8a) and (8b)²¹. We then derive the scattering intensity using the magnetic and electric currents on the virtual surface area s as a function of scattering angles θ and ϕ as follows²¹

$$I(\theta, \phi) = \frac{1}{2\eta_0} (|E_\theta|^2 + |E_\phi|^2) = \frac{k^2}{32\pi^2\eta_0 R^2} (|L_\phi + \eta_0 N_\theta|^2 + |L_\theta - \eta_0 N_\phi|^2). \quad (12)$$

Therefore the scattered power from the material surface corresponding to the virtual surface area s is an integral of the scattering intensity in a half-sphere space over s :

$$\begin{aligned} W_{sca} &= \frac{k^2}{32\pi^2\eta_0 R^2} \int_0^{2\pi} \int_{\pi/2}^{\pi} (|L_\phi + \eta_0 N_\theta|^2 + |L_\theta - \eta_0 N_\phi|^2) R^2 \sin\theta d\theta d\phi \\ &= \frac{k^2}{32\pi^2\eta_0} \int_0^{2\pi} \int_{\pi/2}^{\pi} (|L_\phi + \eta_0 N_\theta|^2 + |L_\theta - \eta_0 N_\phi|^2) \sin\theta d\theta d\phi. \end{aligned} \quad (13)$$

The exact scattering efficiency is $Q_{sca} = \lim_{s \rightarrow \infty} \frac{W_{sca}}{I_0 s}$, where I_0 is the incident intensity.

The Mueller matrix is derived from the amplitude scattering matrix elements. To calculate the amplitude scattering matrix elements, similar to the treatment of Yang and Liou⁴⁰ the scattered field is decomposed into the components parallel and perpendicular to the scattering plane as shown in Fig. 3. So we have

$$\mathbf{E}(\mathbf{R}) = \boldsymbol{\alpha} E_{\alpha}(\mathbf{R}) + \boldsymbol{\beta} E_{\beta}(\mathbf{R}), \quad (14)$$

where $\boldsymbol{\alpha}$ and $\boldsymbol{\beta}$ denote the unit vectors parallel and perpendicular to the scattering plane as shown in Fig. 3, respectively, and $\boldsymbol{\beta} \times \boldsymbol{\alpha} = \mathbf{r}$.

Based on the definition of amplitude scattering matrix, we have the transformation equation for light scattering by surface as

$$\begin{pmatrix} E_{\alpha}(\mathbf{R}) \\ E_{\beta}(\mathbf{R}) \end{pmatrix} = \frac{\exp(-ikR)}{ikR} \begin{bmatrix} s_2 & s_3 \\ s_4 & s_1 \end{bmatrix} \begin{pmatrix} E_{0,\alpha} \\ E_{0,\beta} \end{pmatrix}, \quad (15)$$

where $E_{0,\alpha}$ and $E_{0,\beta}$ are the parallel and perpendicular incident field components with respect to the scattering plane. $E_{0,\alpha}$ and $E_{0,\beta}$ are related to the x -polarized and y -polarized incident fields used in the FDTD simulation with

$$\begin{pmatrix} E_{0,\alpha} \\ E_{0,\beta} \end{pmatrix} = \begin{bmatrix} \boldsymbol{\beta} \cdot \mathbf{x} & -\boldsymbol{\beta} \cdot \mathbf{y} \\ \boldsymbol{\beta} \cdot \mathbf{y} & \boldsymbol{\beta} \cdot \mathbf{x} \end{bmatrix} \begin{pmatrix} E_{0,y} \\ E_{0,x} \end{pmatrix}. \quad (16)$$

Therefore, using Eqs.(8a), (8b), (15), and (16), along with $E_{\theta} = E_{\alpha}$ and $E_{\phi} = -E_{\beta}$, we have the amplitude scattering matrix

$$\begin{bmatrix} s_2 & s_3 \\ s_4 & s_1 \end{bmatrix} = \begin{bmatrix} F_{\alpha,y} & F_{\alpha,x} \\ F_{\beta,y} & F_{\beta,x} \end{bmatrix} \begin{bmatrix} \boldsymbol{\beta} \cdot \mathbf{x} & \boldsymbol{\beta} \cdot \mathbf{y} \\ -\boldsymbol{\beta} \cdot \mathbf{y} & \boldsymbol{\beta} \cdot \mathbf{x} \end{bmatrix}, \quad (17)$$

where the quantities $F_{\alpha,x}$, $F_{\beta,x}$ and $F_{\alpha,y}$, $F_{\beta,y}$ are calculated for x-polarized and y-polarized incident light, respectively, in forms:

(1) For x-polarized incidence,

$$\begin{pmatrix} F_{\alpha,x} \\ F_{\beta,x} \end{pmatrix} = \frac{k^2}{4\pi} \begin{pmatrix} L_\phi + \eta_0 N_\theta \\ L_\theta - \eta_0 N_\phi \end{pmatrix}; \quad (18)$$

(2) For y-polarized incidence,

$$\begin{pmatrix} F_{\alpha,y} \\ F_{\beta,y} \end{pmatrix} = \frac{k^2}{4\pi} \begin{pmatrix} L_\phi + \eta_0 N_\theta \\ L_\theta - \eta_0 N_\phi \end{pmatrix}. \quad (19)$$

Based on these elements of the amplitude scattering matrix, all of the elements of Mueller matrix⁴¹ can be calculated. Since the calculation accuracy of this Mueller matrix is also a function of the virtual surface area s , when s is infinitely large, the Mueller matrix approaches exact. To approximate the infinite-surface Mueller matrix with a limited number of surface periods, we rewrite the relation between incident and scattered Stokes parameters in a new form

$$\begin{bmatrix} I_s/s \\ Q_s/s \\ U_s/s \\ V_s/s \end{bmatrix} = \frac{S_{11}/(k^2 s)}{R^2} \begin{bmatrix} 1 & S_{12}/S_{11} & S_{13}/S_{11} & S_{14}/S_{11} \\ S_{21}/S_{11} & S_{22}/S_{11} & S_{23}/S_{11} & S_{24}/S_{11} \\ S_{31}/S_{11} & S_{32}/S_{11} & S_{33}/S_{11} & S_{34}/S_{11} \\ S_{41}/S_{11} & S_{42}/S_{11} & S_{43}/S_{11} & S_{44}/S_{11} \end{bmatrix} \begin{bmatrix} I_0 \\ Q_0 \\ U_0 \\ V_0 \end{bmatrix}, \quad (20)$$

where I_s/s , Q_s/s , U_s/s , and V_s/s denote the scattered Stokes parameters per unit area of the surface. In Eq.(20), $S_{11}/(k^2 s)$ is a normalized phase function, which accounts for the reflectance at each scattering angle. Therefore the integration of $S_{11}/(k^2 s)$ over the half-space above the scattering surface equals the scattering efficiency (albedo), i.e.

$$\int_0^{2\pi} \int_{\pi/2}^{\pi} [S_{11} / (k^2 s)] \sin \theta d\theta d\phi = Q_{sca}. \quad (21)$$

The normalized phase function needs integral over large s to approach its exact correspondence because of the errors in obtaining the δ factor from limited number of surface periods. However, as previously discussed, the ratios of Mueller matrix elements to S_{11} are not affected by the δ factor and their accuracies are determined simply by the FDTD calculation for single period of the surface.

4. Numerical results

Optical probes for microelectronics manufacturing are gaining increasing importance. Many applications require the characterization of materials and devices such as arrays of nanometer- or micron-sized particles to make crystalline structures, as shown in Fig. 1. Bidirectional reflectance distribution function (BRDF) and bidirectional transmittance distribution function (BTDF) are usually measured to characterize crystalline structures. Numerical calculation of the BRDF or BTDF of crystalline structures can directly link their optical characteristics with their geometric and physical properties. Therefore, numerical simulation of the BRDF or BTDF of material interfaces could be the basis for accurate characterization of crystalline structures. As an example, in this work we calculate the light scattered from and transmitted through a monolayer of micron-sized dielectric spheres on a silicon substrate (See Fig. 1). The spheres on the substrate are touching and in a hexagonal configuration. Although the simplest base for this crystalline structure is hexagonal, as shown in Fig. 4, we can use a periodic rectangular grid with a sphere in the center and the rectangular box passing through the centers of the adjacent spheres for the FDTD calculation to simulate the light scattering and transmission by the surface structure. In this simulation, the incident wavelength is $\lambda_0 = 308 \text{ nm}$, and the

refractive indices of the spheres and the silicon substrate are $m = 1.64$ and $m = 4.90 + 3.84i$, respectively. The radii of the spheres are 510 nm . We are interested in both the near-fields transmitted in the silicon substrate and the far-fields scattered by the sphere-substrate system in free space. In the FDTD calculations, we use a 6-cell UPML to truncate the free space and a 6-cell UPML on the other end to truncate the material space. The cubic spatial cell size for the FDTD is set to be $\Delta s = \lambda_0 / 60$. For comparison with the light scattering features of the system of the silicon substrate and the micron-sized spheres, the normalized phase function and the Mueller matrix elements of the simple flat substrate are also calculated.

Figure 5 shows the azimuthally averaged normalized light scattering phase function of the flat silicon substrate under normal incidence. For this flat surface scattering calculation, the FDTD simulation is run on a 308 nm by 308 nm substrate period. The transformation of near-field to far-field is done with integration of the near fields over 2001-by-2001 periods of the surface. We can see that most of the scattered energy concentrates in a very small solid angle around the backscattering direction (i.e., at a scattering angle of 180°). However, due to limited periods of surface are used to approximate the normalized phase function, small amount of scattered energy can still be found at other scattering angles, although that intensity is several orders lower than the backscattered peak. The small scattered intensity at other scattering angles demonstrates strong variations, but their envelopes form a smooth slope which can be measured. For light scattering by the system of the monolayer of spheres and the silicon substrate (Fig. 6), the azimuthally averaged normalized light scattering phase function has two specific maxima (numbered 2 and 3) at the scattering angles of $\sim 115^\circ$ and $\sim 145^\circ$, respectively.

These maxima are because of the side-scattering by the spheres on the substrate and may be used in characterization of the feature of the system. However, for characterization of this kind of system the polarization features of scattered light might contain the most useful information. Figs. 7(a)-(c) show the nonzero azimuthally averaged normalized Mueller matrix elements of the system of the monolayer of spheres and the silicon substrate. Also shown in these figures are the results for light scattered simply by the flat substrate. We can see that the polarization degrees of the scattered light from simply the flat substrate and from the substrate with the spherical particles are significantly different. At the scattering angle of $\sim 115^\circ$, $S_{12}(S_{21}) / S_{11}$, $S_{33}(S_{44}) / S_{11}$, and $S_{34}(-S_{43}) / S_{11}$ all show a strong peak corresponding to maxima 3 as shown in Fig. 6. Because these quantities are independent on the number of periods in the near-field to far-field transformation integration, their accuracies in the numerical calculation are high and solely determined by the FDTD technique. Furthermore, corresponding to maxima 2 in Fig. 6, $S_{12}(S_{21}) / S_{11}$, $S_{33}(S_{44}) / S_{11}$, and $S_{34}(-S_{43}) / S_{11}$ all have maxima, especially in the linear polarization degree $S_{12}(S_{21}) / S_{11}$. This polarization feature of scattered light could easily be detected by polarimetry.

For light transmitted through the monolayer of spheres, we calculate the energy flux $\lambda_0 / 30$ deep inside the substrate for a period of the surface system. Figure 8 shows the spatial distribution of the transmitted flux normalized by the incident flux. We can see that the transmitted energy focuses around the ray passing through centers of the spheres. At other locations, the transmitted flux is very small. Therefore, a transmitted laser light distributed by the micron-sphere structures can make nanometer-sized structures on the

substrate, which have been observed by atomic force microscopy (Erhard Rothe, personal communications).

5. Summary and Conclusions

In this study, we have incorporated periodic boundary conditions into the finite-difference time-domain algorithm to enable it to calculate scattering from periodic systems, especially structure or roughness on substrates. With some care this algorithm can also be employed to calculate the scattering from isolated structures on an infinite substrate. In such cases the enclosed discretized volume should be chosen so that there is large enough separation between the simulated periodic structures that the interaction between them is negligible. Experimental measurements have shown that such a volume is rather small, especially with regards to the TE incidence.⁴² In this case the far-field can be determined by integrating over the single near-field perturbation from the system of a plane substrate. For such isolated systems, we are not restricted to specific discrete incident angles, since the size of the volume can be varied to select the required incident angle; i.e., $m\lambda_0 = D \sin \theta_0$ where D is the length of the substrate under consideration and m is an integer.

We have applied the finite-difference time-domain technique to calculate the scattered and transmitted electromagnetic fields near a period of an infinite periodic rough surface. The elements of Mueller matrix for scattered light are calculated by an integral of the near fields over a significant number of periods of the surface. The normalized Mueller matrix elements of the scattered light and the field density of transmitted light for a monolayer of dielectric spheres on a silicon substrate are calculated. The numerical results show that the nonzero Mueller matrix elements of the system of a monolayer of

dielectric spheres on a silicon substrate have two specific maxima at the scattering angles of $\sim 115^\circ$ and $\sim 145^\circ$, respectively. These maxima may be used in characterization of the system. For light transmitted through the monolayer of spheres, our results show that the transmitted energy focuses around the ray passing through centers of the spheres. At other locations, the transmitted flux is very small.

Acknowledgment

The authors thank Erhard Rothe of Wayne State University for helpful communications on the sphere-substrate structures.

References

1. D. L. Schuler, J.-S. Lee, D. Kasilingam, and G. Nesti, "Surface roughness and slope measurements using polarimetric SAR data," *IEEE Transactions on Geoscience and Remote Sensing* **40**, 687-698 (2002).
2. S. Gomez, K. Hale, J. Burrows, and B. Griffiths, "Measurements of surface defects on optical components," *Meas. Sci. Technol.* **9**, 607-616 (1998).
3. H. Lin and J. Zhu, "Characterization of nanocrystalline silicon films," *Proc. SPIE* **4700**, 354-356 (2002).
4. H. Budiarto and J. Takada, "The electromagnetic wave scattering from building surfaces for the mobile propagation modeling," *ITE Technical Report* **25**, 7-11 (2001).
5. Lord Rayleigh, *The theory of sound* (MacMillan, London, 1896).
6. U. Fano, "The theory of anomalous diffraction gratings and of quasi-stationary waves on metallic surfaces (Sommerfeld's waves)," *J. Opt. Soc. Am.* **31**, 213-222 (1941).
7. S. O. Rice, "Reflection of electromagnetic waves from slightly rough surfaces," *Commun. Pure Appl. Math.* **4**, 351-378 (1951).
8. S. O. Rice, *Reflection of EM from slightly rough surfaces* (Interscience, New-York, 1963).
9. C. Eckart, "The scattering of sound from the sea surface," *J. Acoust. Soc. Am.* **25**, 66-570 (1953).
10. H. Davies, "The reflection of electromagnetic waves from rough surfaces," *Proc. IEE (London)* **101**, 209-214 (1954).

11. P. Beckmann and A. Spizzichino, *The scattering of electromagnetic waves from rough surfaces* (Pergamon Press, Oxford, England, 1963).
12. A. K. Fung and G. W. Pan, "An integral equation method for rough surface scattering," in *Proceedings of the International Symposium on multiple scattering of waves in random media and random surfaces*, 701–714 (1986).
13. A. K. Fung, Z. Li, and K. S. Chen, "Backscattering from a randomly rough dielectric surface," *IEEE Trans. Geosci. and Remote Sens.* **30**, 356–369 (1992).
14. A. K. Fung, *Microwave scattering and Emission Models and their Applications* (Artech House, Norwood, Massachusetts, 1994).
15. L. Tsang, J. A. Kong, K. H. Ding, and C. O. Ao, *Scattering of electromagnetic waves: Numerical simulations* (Wiley, New York, 2001).
16. M. Saillard and A. Sentenac, "Rigorous solutions for electromagnetic scattering from rough surfaces," *Waves in Random Media* **11**, 103-137 (2001).
17. P. P. Silvester and R. L. Ferrari, *Finite elements for electrical engineers* (Cambridge Univ. Press, Cambridge, U.K., 1990).
18. J. M. Jin, *The finite element method in electromagnetics* (Wiley, New York, 1993).
19. K. S. Yee, "Numerical solution of initial boundary value problems involving Maxwell's equations in isotropic media," *IEEE Trans. Antennas Propagat.* **14**, 302-307 (1966).
20. K. S. Kunz and R. J. Luebbers, *The Finite Difference Time Domain Method for Electromagnetics* (CRC Press, Boca Raton, FL, 1993).

21. A. Taflove, *Computational Electrodynamics: The Finite-Difference Time-Domain Method* (Artech House, Boston, MA, 1995).
22. C. Y. Hsieh, A. K. Fung, G. Nesti, A. J. Siber, and P. Coppo, "A further study of the IEM surface scattering model," *IEEE Trans. Geosci. and Remote Sens.* **35**, 901–909 (1997).
23. A. K. Fung, Z. Li, and K. S. Chen, "An improved IEM model for bistatic scattering from rough surfaces," *J. Electromagn. Waves and Appl.* **16**, 689–702 (2002).
24. K. S. Chen, T. D. Wu, and A. K. Fung, "A study of backscattering from multi-scale rough surface," *J. Electromagn. Waves and Appl.* **12**, 961–979 (1998).
25. F. Mattia, "Backscattering properties of multi-scale rough surfaces," *J. Electromagn. Waves and Appl.* **13**, 493–527 (1999).
26. C. H. Chan, S. H. Lou, L. Tsang, and J. A. Kong, "Electromagnetic scattering of waves by rough surfaces: A finite-difference time-domain approach," *Microwave Opt. Technol. Lett.* **4**, 355–359 (1991).
27. A. K. Fung, M. R. Shah, and S. Tjuatja, "Numerical simulation of scattering from three-dimensional randomly rough surfaces," *IEEE Trans. Geosci. Remote Sensing* **32**, 986–994 (1994).
28. F. D. Hastings, J. B. Schneider, and S. L. Broschat, "A Monte-Carlo FDTD technique for rough surface scattering," *IEEE Trans. Antennas Propagat.* **43**, 1183–1191 (1995).
29. R. J. Luebbers and C. Penney, "Scattering from apertures in infinite ground planes using FDTD," *IEEE Trans. Antennas Propagat.* **42**, 731–736 (1994).

30. K. Demarest, R. Plumb, and Z. Huang, "FDTD modeling of scatterers in stratified media," *IEEE Trans. Antennas Propagat.* **43**, 1164-1168 (1995).
31. P. B. Wong, G. L. Tyler, J. E. Baron, E. M. Gurrola, and R. A. Simpson, "A three-wave FDTD approach to surface scattering with applications to remote sensing of geophysical surfaces," *IEEE Trans. Antennas Propagat.* **44**, 504-513 (1996).
32. Z. S. Sacks, D. M. Kingsland, R. Lee, and J.-F. Lee, "A perfectly matched anisotropic absorber for use as an absorbing boundary condition," *IEEE Trans. Antennas Propagat.* **43**, 1460-1463 (1995).
33. S. D. Gedney, "An anisotropic perfectly matched layer-absorbing medium for the truncation of FDTD lattices," *IEEE Trans. Antennas Propagat.* **44**, 1630-1639 (1996).
34. A. Taflove and M. E. Brodwin, "Numerical solution of steady-state electromagnetic scattering problems using the time-dependent Maxwell's equations," *IEEE Trans. Microwave Theory Tech.* **MTT-23**, 623-630 (1975).
35. W. Sun, Q. Fu, and Z. Chen, "Finite-difference time-domain solution of light scattering by dielectric particles with a perfectly matched layer absorbing boundary condition," *Appl. Opt.* **38**, 3141-3151 (1999).
36. D. E. Merewether, R. Fisher, and F.W. Smith, "On implementing a numeric Huygen's source in a finite difference program to illustrate scattering bodies," *IEEE Trans. Nucl. Sci.* **NS-27**, 1829-1833 (1980).

37. K. Umashanker and A. Taflove, "A novel method to analyze electromagnetic scattering of complex objects," *IEEE Trans. Electromagn. Compat.* **EMC-24**, 397-405 (1982).
38. A. Taflove, *Computational Electrodynamics: The Finite-Difference Time Domain Method* (Artech House, Boston, 1995).
39. W. Sun, N. G. Loeb, and Q. Fu, "Finite-difference time domain solution of light scattering and absorption by particles in an absorbing medium," *Appl. Opt.* **41**, 5728-5743 (2002).
40. P. Yang and K. N. Liou, "Finite-difference time domain method for light scattering by small ice crystals in three-dimensional space," *J. Opt. Soc. Am. A* **13**, 2072-2085 (1996).
41. C. F. Bohren and D. R. Huffman, *Absorption and Scattering of Light by Small Particles* (Wiley, New York, 1983).
42. F. Moreno, F. Gonzalez, J. M. Saiz, P. J. Valle, D. L. Jordan, "Experimental study of copolarized Light scattering by spherical metallic particles on conducting flat substrates," *J. Opt. Soc. Am. A* **10**, 141-149 (1993).

Figure Captions

1. Illustration of a monolayer of dielectric spheres on a silicon substrate and the coordinate system used in this study.
2. Illustration of implementing the FDTD algorithm for calculation of the scattered and transmitted fields near a periodic rough surface.
3. Geometry for the derivation of the amplitude scattering matrix elements
4. Geometry of one period in the system of a monolayer of dielectric spheres on a silicon substrate.
5. Normalized light scattering phase function $S_{11}/(k^2s)$ of the flat silicon substrate.
6. Normalized light scattering phase function $S_{11}/(k^2s)$ of a monolayer of dielectric spheres on a silicon substrate.
7. Normalized Muller matrix elements of the monolayer of dielectric spheres on a silicon substrate under normal incidence: (a) S_{12} (S_{21}) / S_{11} , (b) S_{33} (S_{44}) / S_{11} , and (c) S_{34} ($-S_{43}$) / S_{11} . Also shown are the corresponding normalized Muller matrix elements of the flat silicon substrate in dashed line.
8. Normalized transmitted light flux at a depth of $\lambda_0/30$ inside the silicon substrate for a period of the rough surface system as shown in Fig. 4.

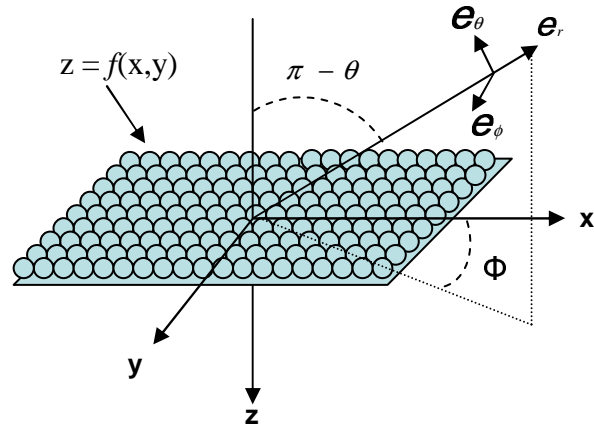


Fig. 1 of Sun et al.

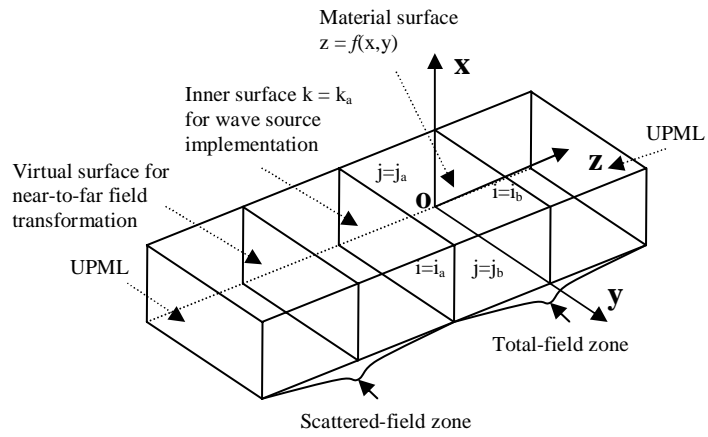


Fig. 2 of Sun et al.

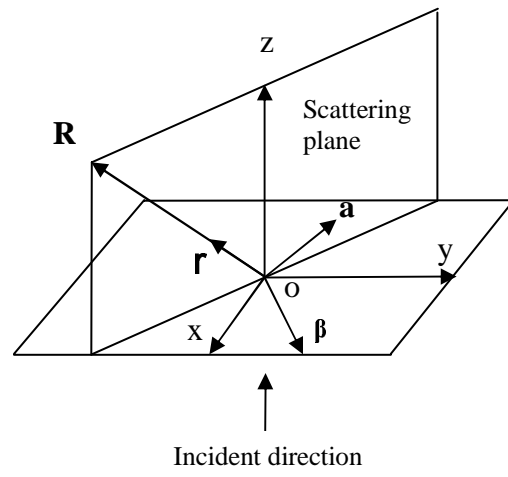


Fig. 3 of Sun et al.

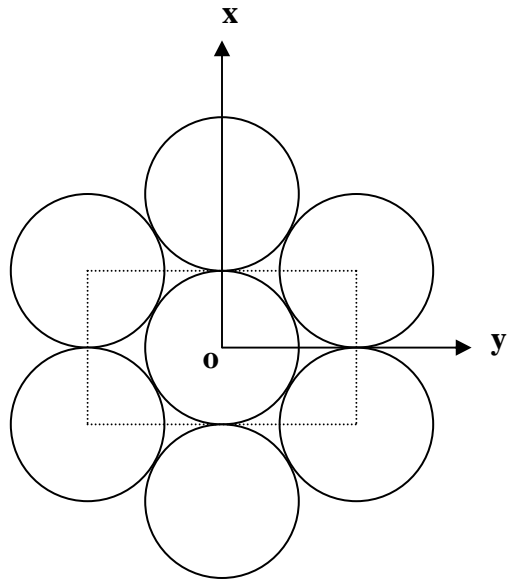


Fig. 4 of Sun et al.

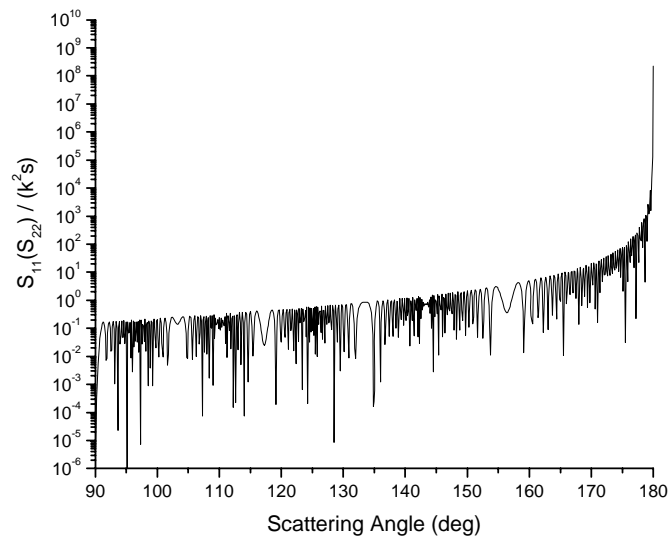


Fig. 5 of Sun et al.

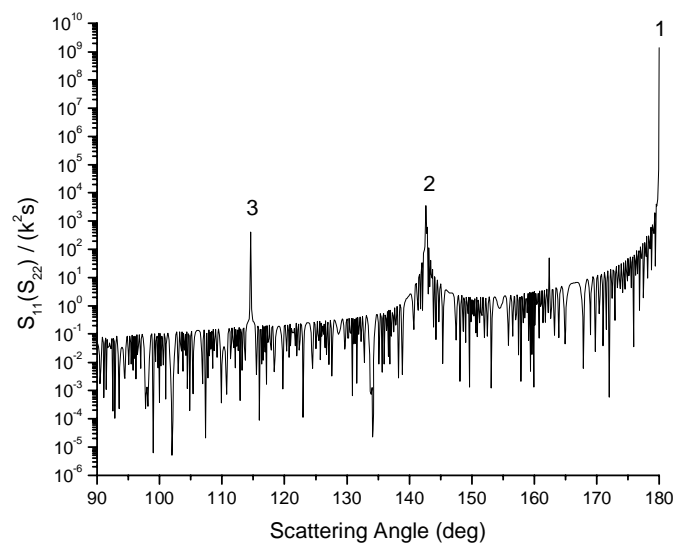


Fig. 6 of Sun et al.

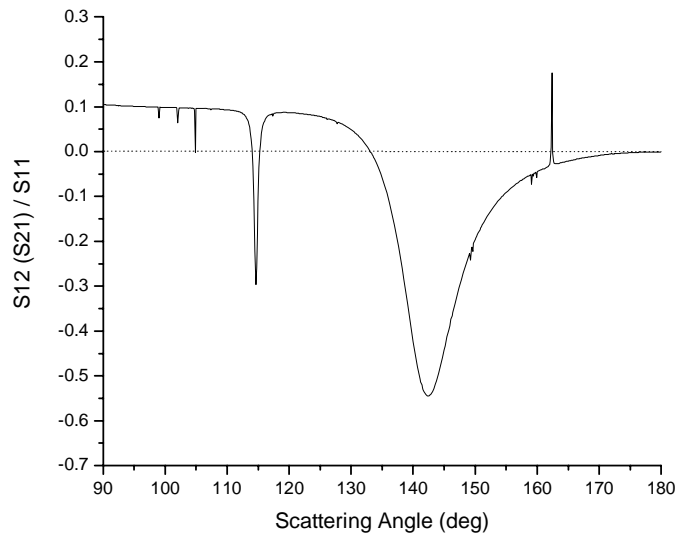


Fig. 7 (a) of Sun et al.

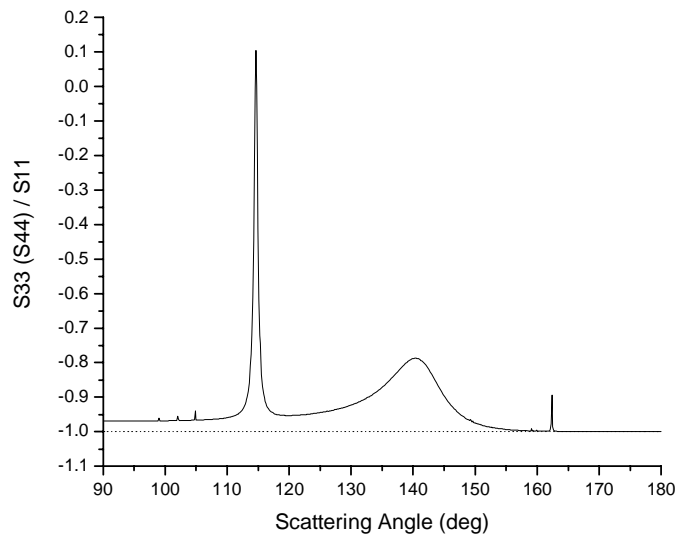


Fig. 7 (b) of Sun et al.

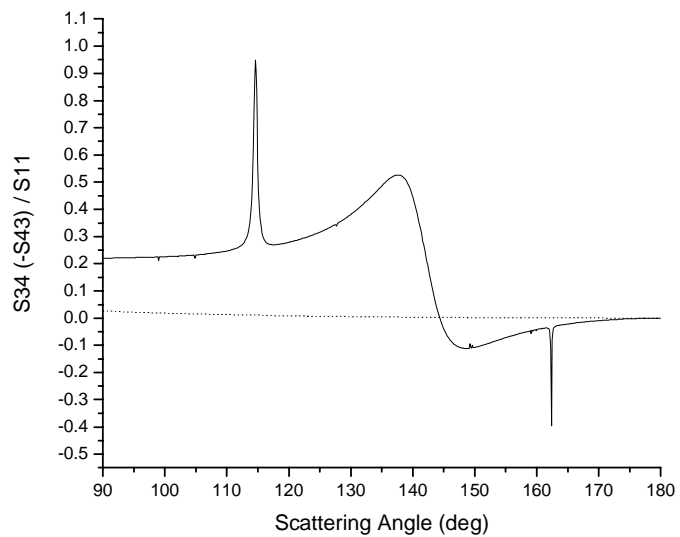


Fig. 7(c) of Sun et al.

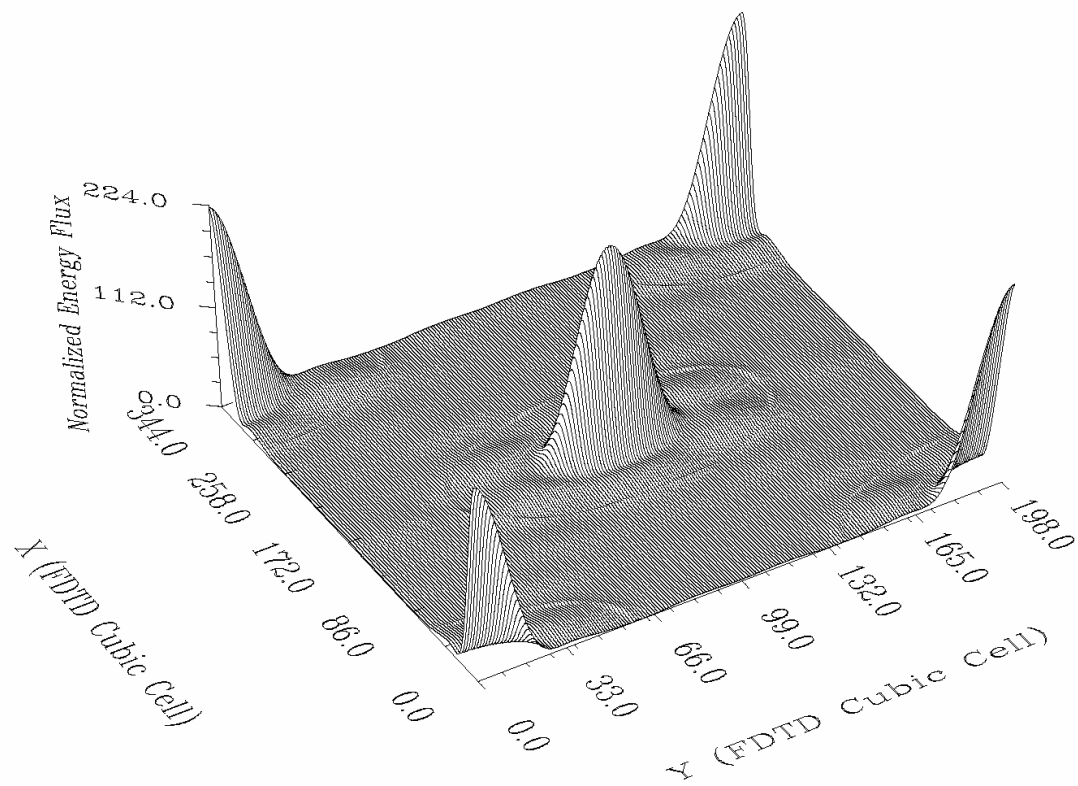


Fig. 8 of Sun et al.